Chemical Engineering Journal 512 (2025) 162513

Contents lists available at ScienceDirect

Chemical Engineering Journal

journal homepage: www.elsevier.com/locate/cej

Engineering strategies to minimize bubble-induced optical losses in photoelectrochemical water splitting

Feng Liang [a], Roel van de Krol [a,b], Fatwa F. Abdi [a,c,*]

[a] Institute for Solar Fuels, Helmholtz-Zentrum Berlin für Materialien und Energie GmbH, Hahn-Meitner-Platz 1, 14109 Berlin, Germany
[b] Department of Chemistry, Technische Universität Berlin, Straße des 17. Juni 124, 10623 Berlin, Germany
[c] School of Energy and Environment, City University of Hong Kong, 83 Tat Chee Avenue, Kowloon, Hong Kong SAR, China

ARTICLE INFO

Keywords:
Photoelectrochemical water splitting
Bubbles
Shadowgraphy
Pressure elevation
Bubble-induced optical loss

ABSTRACT

Gas bubble evolution presents a significant challenge to achieving efficient solar water splitting by blocking catalytic active sites, increasing electrolyte ohmic resistance, and scattering incident solar photons. The bubble-induced optical loss is especially important in photoelectrochemical (PEC) cells, as specific cell configurations require light to travel through the electrolyte before reaching the photoelectrodes. Understanding bubble characteristics under various operating conditions and the associated bubble-induced optical losses is essential to optimize the PEC water splitting efficiency. In this study, we use optical measurements and bubble shadowgraphy to demonstrate that operating PEC water splitting systems at elevated pressure (up to 4 bar) reduces bubble-induced optical losses by a factor of four, with only a minimal (~1%) increase in thermodynamic cell voltage. In addition, lowering the electrolyte buffer concentration further mitigates the bubble-induced optical losses, albeit at the cost of increased overpotential due to higher ohmic resistance and increased adhesion of the larger bubbles. These quantitative results provide valuable insights into the design and practical implementation of PEC water splitting cells, and the approach can be extended to other gas-evolving photoelectrochemical conversion systems.

1. Introduction

In the quest for sustainable energy solutions, photoelectrochemical (PEC) water splitting offers a direct and environmentally friendly pathway for harnessing abundant and renewable sunlight to produce hydrogen [1–4]. Significant progress has been made in developing highly efficient light-absorbing semiconductors and electrocatalysts [2,5–10]. However, device engineering remains one of the major bottlenecks in bridging the gap between laboratory studies and practical applications [11–20]. Substantial efforts have been invested in improving photoelectrode and/or cell efficiency through designing cell architectures that minimize optical losses [12,13], improving photocurrents [17], and alleviating kinetic overpotential losses [15,16,21], but relatively little attention has been given to the losses associated with the hydrogen and oxygen gas bubbles that evolve on the photoelectrode surfaces. This oversight is perhaps not surprising since bubble-induced ohmic and active surface area losses in PEC water splitting cells are typically not the main performance loss factors at the relatively low current densities (< 20 mA cm^{-2}) reported for most studies. In contrast, bubble dynamics in nonilluminated electrochemical systems (e.g., dark electrolyzers) have been extensively studied. These systems operate at high current densities (up to several A cm^{-2}), and the presence of large amounts of bubbles increases the ohmic resistance and reduces the electrochemically active area [22,23]. As a result, the (over)potential required to drive the electrochemical reaction kinetics increases and the device efficiencies are reduced [24,25]. At the same time, bubbles also offer benefits in such systems by passively aiding product separation [26] and/or enhancing mass transport to the electrode surface [27]. The latter is especially beneficial when a neutral pH buffer solution is used, as bubble-induced convection can minimize the local pH gradients and the associated overpotentials [28].

Despite the relatively minor effect of bubble-induced ohmic and surface coverage losses in PEC water splitting cells, the optical losses caused by bubble scattering are not necessarily insignificant and could be challenging to quantify [29,30]. In most PEC device configurations [31], light needs to pass through the electrolyte and the gas bubbles before reaching the semiconductor photoelectrode. Due to the relatively smooth bubble/electrolyte interface and the refractive index mismatch,

---

[*] Corresponding author at: School of Energy and Environment, City University of Hong Kong, 83 Tat Chee Avenue, Kowloon, Hong Kong SAR, China.
E-mail address: ffabdi@cityu.edu.hk (F.F. Abdi).

https://doi.org/10.1016/j.cej.2025.162513
Received 2 February 2025; Received in revised form 4 April 2025; Accepted 9 April 2025

a fraction of photons is lost through reflection and refraction [30]. Depending on the cell configuration, there are two general scenario of gas bubbles altering the light path. First, light needs to transmit through the gas bubble floating in the electrolyte before reaching the photoabsorbers. Second, light may have to pass through adhered gas bubbles before being absorbed by the photoelectrodes. In the first scenario, multiple reflection and refraction at gas/electrolyte interfaces may occur, complicating the overall process but likely to cause more optical loss. In the second case, despite light being re-directed (or re-distributed) by the bubble/electrolyte interface, the proximity of the bubbles from the photoabsorbers means that not all light is necessarily lost. These two scenarios often co-exist in PEC water splitting measurement, which further complicates the quantitative assessment of bubble-induced optical loss.

A (limited) number of quantitative studies of bubble evolution in PEC cells have been reported. For example, Hu et al. reported that the photocurrent of a nanostructured TiO_2 photoanode fluctuated by ∼ 7 % due to the periodic bubble evolution [32]. In addition, an investigation of losses induced by single hydrogen bubble using *in situ* scanning photocurrent microscopy (SPCM) revealed that the optical loss increased up to 23 % at larger bubble size [33]. A Monte Carlo ray-tracing simulation showed that the area-averaged absorptance in a bubble-covered Si photoelectrode was reduced by up to 18 % compared to a bare photoelectrode [34]. In contrast, other studies have reported relatively minor optical losses. For example, small oxygen bubbles on upward-facing, cm-scale illuminated silicon photoelectrodes induced minimal optical losses, especially at increased electrolyte flow rates [35]. Experiments using transparent, non-photoactive electrodes also reported moderate losses; a population of bubbles evolving from a transparent conducting electrode (F-doped SnO_2) caused optical losses of ∼ 5 % at current densities up to 8 mA cm^{-2} [30]. Overall, these conflicting results highlight the complexity of bubble-induced optical effects in PEC cells. The divergence in findings suggest that bubble-induced optical losses largely depend on experimental conditions, complicating efforts in generalizing their impact.

In this study, we investigate the scattering-induced optical losses for H_2 and O_2 bubbles in a water splitting cell operating at typical PEC current densities and at moderately elevated pressure (up to 4 bar). The generation of pressurized green H_2 from a PEC water splitting cell has recently be reported as a promising technological pathway as it reduces the need for mechanical compression in downstream chemical processes [29,36]. Furthermore, our multiphysics modeling based evaluation identified that bubble-induced optical loss can contribute up to ∼ 50 % of the total loss during PEC water splitting at 1 bar [36]. Elevated pressure is expected to reduce bubble-induced losses as the bubble size is reduced and dissolved gas concentrations increase with pressure [37–39]. Herein, we conduct quantitative investigations on bubble-induced optical loss at moderately elevated pressure, focusing on systems using potassium phosphate (KP_i) buffer at near-neutral pH, as this electrolyte is used in many PEC studies. Unlike previous reports that primarily focused on the effects of adhered bubbles, our study emphasizes the optical effect of mobile bubbles within the electrolyte. By measuring transmitted optical power and capturing shadowgraphs of bubbles using macroscopic imaging, we quantitatively assess the relationship between bubble characteristics (e.g., average bubble diameter, number of bubbles per frame, bubble formation efficiency) and the optical power loss at various pressures, current densities, and KP_i buffer concentrations. Finally, our findings allow us to propose practical strategies to mitigate bubble-induced loss in PEC water splitting systems.

2. Results and discussions

2.1. *Effect of H_2 and O_2 bubble evolution on the optical loss*

Fig. 1a shows the schematic depiction of our experimental setup, where the impact of bubble evolution on the optical losses under simulated sunlight illumination was measured using a thermopile sensor. Bubble evolution was controlled by galvanostatic operation of an electrochemical water splitting cell, which consists of a Pt mesh working electrode (WE), a Pt wire counter electrode (CE), and an Ag/AgCl reference electrode in a three-electrode configuration. Experiments were performed at ± 1.2, ±1.9, and ± 2.5 mA cm^{-2} in 0.5, 1.0, and 2.0 M KP_i (pH = 7), and the operating pressure of the cell varied from 1 to 4 bar. Positive currents were applied to the WE to measure the impact of O_2 bubbles, while negative currents were used to measure the impact of H_2 bubbles. Note that although dark electrodes were used in our experiments, the operational conditions were adjusted to reflect those typically used in PEC systems, which makes our findings relevant for PEC water splitting cells. The Pt wire was arranged such that any bubble evolution from the CE does not block the light transmitted towards the thermopile power sensor. Bubble shadowgraphy measurements were conducted with the same setup and parameters, but the thermopile sensor was replaced by a macroscopic camera lens, as shown in Fig. 1b. Note that the camera frame rate was intentionally set to 1 fps since the primary focus of our study is to correlate the optical loss with the averaged bubble characteristics over a relatively large area (cm-scale electrode) at equilibrium. Therefore, the ‘localized’ effects of bubble nucleation, adhesion on the electrode surface, bubble growth, coalescence, and detachment on light transmission, and the mass transfer across the bubble/electrolyte interface are not considered here, despite acknowledging that they are undoubtedly important. Simulating these localized processes on multiple bubbles over a relatively large area is extremely costly and beyond the scope of this study. However, several excellent studies have already been reported in the community that provide detailed insights into gas bubble-electrolyte interaction [40–42]. These works can be referred to for a more comprehensive understanding of how gas bubble dynamics influence local mass transport near the (photo)electrode. Furthermore, other bubble parameters, such as coverage on the Pt electrode, are excluded from our analysis due to the challenges in accurately measuring bubble coverage on curved electrode surfaces. Nevertheless, since the experimental conditions are consistent across all tests, relative comparisons between our experimental results remain valid. A detailed description of the setup is provided in the *Methods* section, and digital photographs of the experimental setup are shown in Fig. S1.

The optical power transmitted through the cell, as measured by the thermopile sensor, is plotted as a function of time (t) in Fig. 2a. For the first ∼ 2 mins of measurements, no bubbles were generated, and the cell was at 1 bar. The average optical power measured under this condition is defined as the background optical power. At t = ∼2 mins, a current density of + 2.5 mA cm^{-2} was applied; O_2 bubbles were generated from the Pt mesh, and the measured optical power decreased. The operating pressure was increased from 1 bar to 2, 3 and 4 bar at t = ∼10, 20, and 28 mins, respectively. At t = ∼38 mins, the operating pressure was set back to 1 bar to check for reproducibility. A similar plot for the case of H_2 bubbles generated from the Pt mesh (at current density of –2.5 mA cm^{-2}) is shown in Fig. 2b. The average values of the optical power at each pressure (upon reaching steady state) are plotted in Fig. 2c. By comparing these optical powers to the background optical power, the bubble-induced optical losses can be quantified (Fig. 2d). At 1 bar, the presence of O_2 and H_2 bubbles each resulted in an optical loss of ∼ 20 %. Increasing the operating pressure significantly reduces these losses. In the case of O_2 bubbles, the losses decreased to ∼ 6 % at 4 bar. A major suppression occurred already when the pressure is increased from 1 to 2 bar with the losses already halved to ∼ 10 %. Similar observations were found when H_2 bubbles were generated, although the effect is less pronounced; the bubble-induced optical losses decreased to ∼ 10 % at 4 bar. The wavelength dependence of O_2 and H_2 bubble scattering was also investigated using a transmittance measurement setup (see Supplementary note 1 and Fig. S2a for details). Within the pressure range tested, the bubble-induced optical losses are independent of wavelength for both O_2 and H_2, as shown in Fig. S2b–S2e.

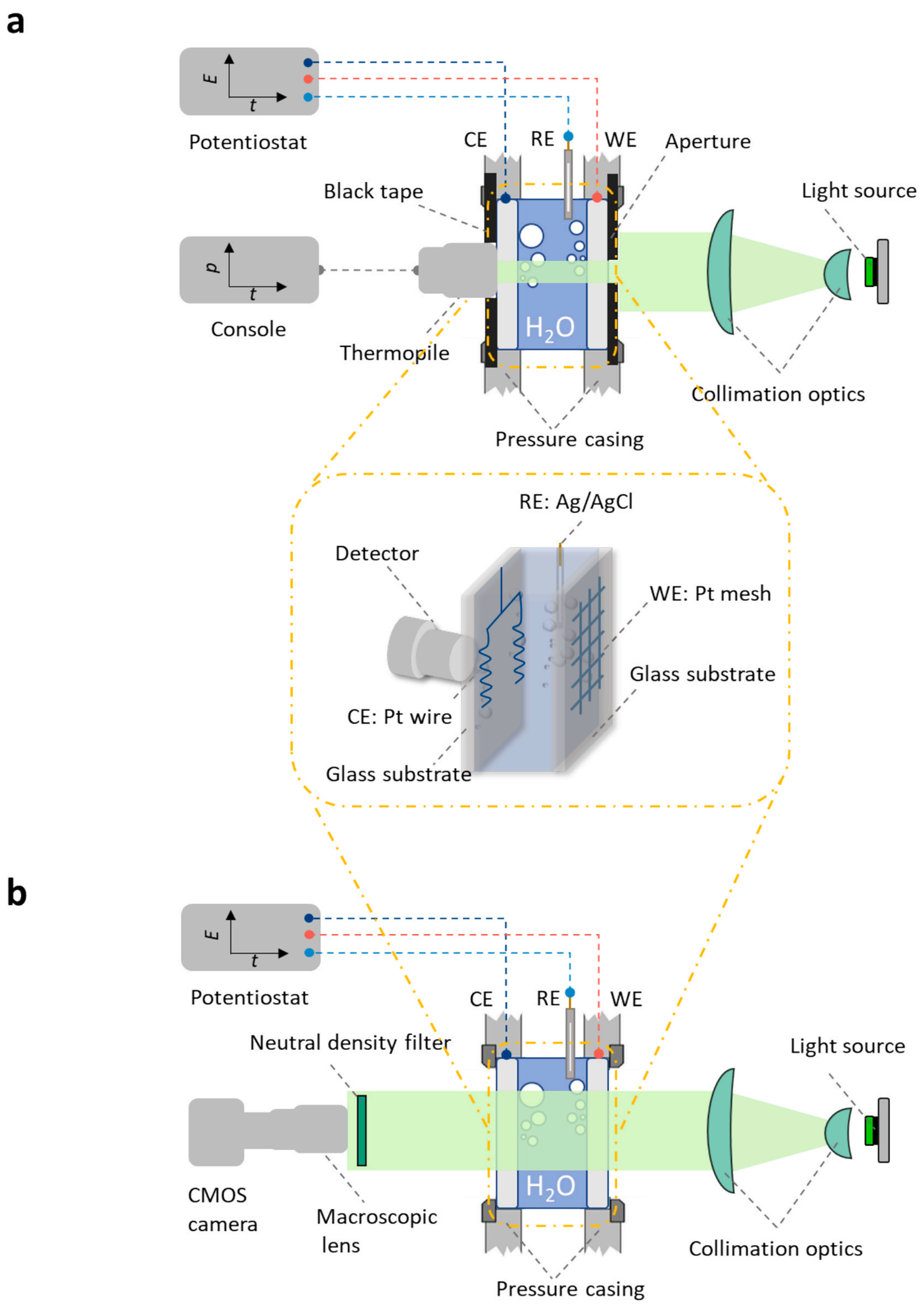

Fig. 1. Schematic illustrations of the (a) bubble optical transmission and (b) bubble shadowgraphy experimental setups. The detector in the inset of (a) indicates either the thermopile sensor or camera lens. In all experiments, a platinum mesh fixed on the transparent glass window of the cell is used as the working electrode (WE) for H_2 or O_2 bubble evolution. The geometric area of the sample is 2 × 2 cm, whereas the actual surface area of the platinum mesh is $\sim 8.8\ cm^2$. The geometric area ($4\ cm^2$) was used to calculate the current density. A miniature Ag/AgCl electrode was used as the reference electrode (RE), and a platinum coil, bend into a shape that does not optically obstruct the measurements (see inset of (a)), was used as the counter electrode (CE). Pressures of up to 4 bar were realized by introducing N_2 (unless otherwise mentioned) into the space at the top of the cell while the outlet flow rate was regulated with a back-pressure controller. Such a configuration minimizes the disturbance to the bubbles/optical power measurements, as illustrated in Fig. S1c. Additionally, the interaction between the O_2 and H_2 bubble plumes can be safely neglected, as the two gas-evolving electrodes were spaced relatively far apart (~3 cm), as indicated in Fig. S1c. The pressure range in our current setup is constrained by the durability of the glass substrates (30 mm × 30 mm × 2.2 mm); these substrates frequently crack at pressures exceeding 4 bar.

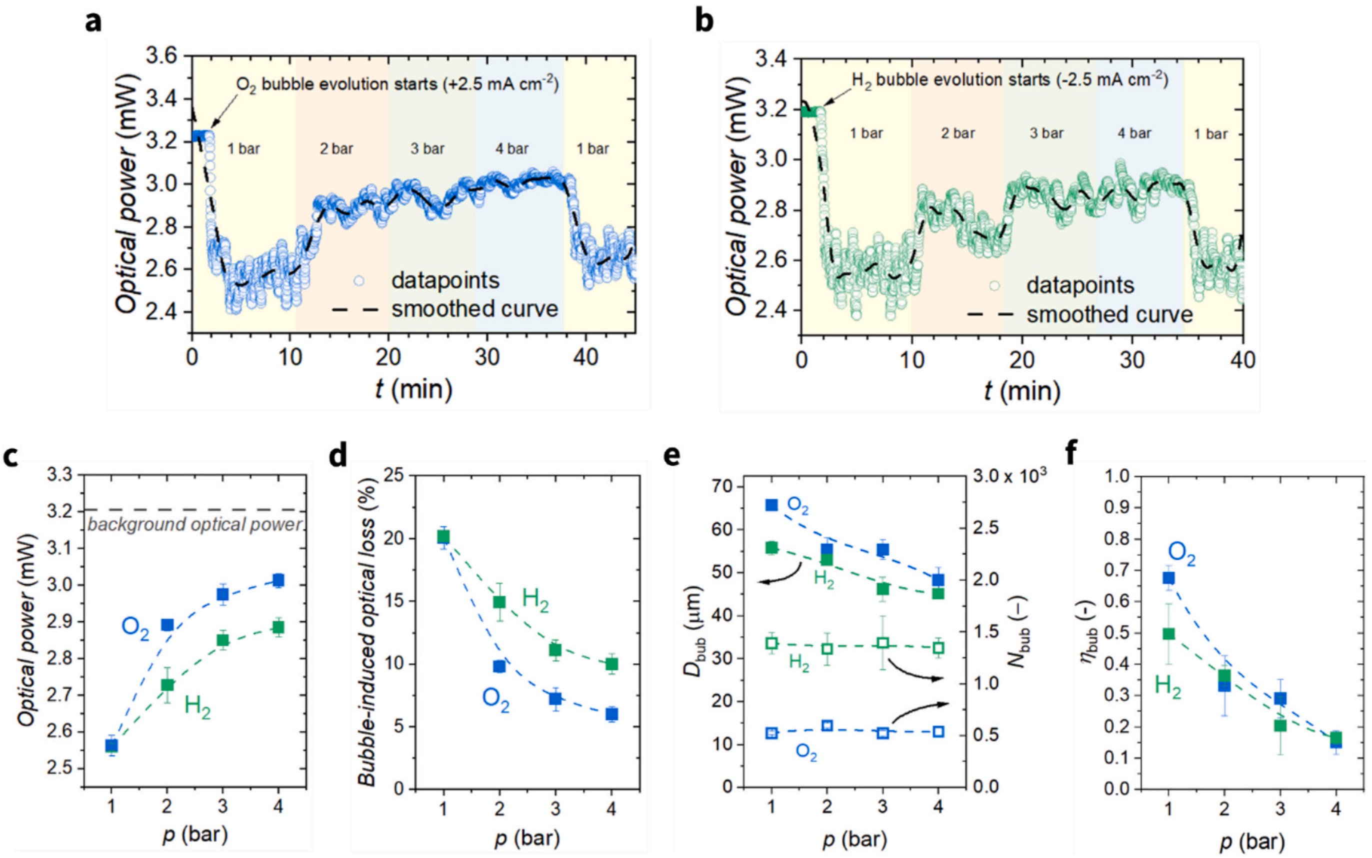

Fig. 2. Measured optical power before and during the galvanostatic operation of the Pt mesh electrode generating (a) O_2 and (b) H_2 bubbles at different pressure. The region in the plot with different pressure are shaded in different colors for better visualization. (c) The average value of transmitted optical power and (d) the corresponding percentage of bubble-induced optical loss at the steady state for each pressure (average of measured values during the last 5 min before the pressure was increased to the next higher level). (e) The average bubble diameter and the number of H_2 and O_2 bubbles at different pressure. (f) Bubble formation efficiency (η_{bub}) of H_2 and O_2. An aqueous solution of 2.0 M KP_i (pH = 7) was used as electrolyte, the current density was ± 2.5 mA cm^{-2} (positive for O_2 bubble evolution, and negative for H_2 bubble evolution), Ag/AgCl was used as the reference electrode, and Pt wire was used as the counter electrode. Error bars represent the standard deviation of at least three tests.

We speculated two possible reasons for the reduction in bubble-induced optical losses at increased pressure. First, an increase in pressure reduces the average bubble size, leading to smaller bubbles that scatter less light. Second, fewer bubbles are formed at elevated pressure due to an increase in the dissolved gas concentration in the electrolyte solution. To test these hypotheses, we performed bubble shadowgraphy to measure bubble characteristics at different pressures. We first calculated the average bubble diameter (D_{bub}) from the shadowgraphs as a function of pressure, as shown in Fig. 2e. Examples of O_2 bubble shadowgraphs can be seen in Fig. S3 and Supplementary video S1. As the pressure increased from 1 to 2 bar and then to 4 bar, the D_{bub} of O_2 bubbles decreased from ~ 65 μm to ~ 55 μm and ~ 48 μm (i.e., by ~ 15 % and ~ 25 %, respectively). A similar trend was also observed for the D_{bub} of H_2 bubbles. Fig. 2e also shows the number of bubbles (N_{bub}) obtained from the shadowgraphs. Surprisingly, N_{bub} for both O_2 and H_2 bubbles is nearly independent of pressure, contrasting with another study that reported the number of bubbles to increase proportionally with pressure [38]. We attribute this difference to the limitations of our macroscopic camera lens (since our study focuses on average bubble characteristics on a cm-scale electrode, a microscopic lens was not used). Our macroscopic lens captures bubbles with a minimum diameter of ~ 30 μm. We believe this resolution is adequate, as a recent *in situ* scanning photocurrent microscopy (SPCM) study reported that bubble-induced external quantum efficiency (EQE) losses decrease with smaller bubbles and bubbles with a size of ~ 150 μm only cause ~ 2.2 % EQE loss [33]. To further rationalize the relationship between pressure-induced reduction in optical scattering and the average bubble size, we calculated the bubble formation efficiency (η_{bub}) for H_2 and O_2 at different pressures, as shown in Fig. 2f. η_{bub} is defined as the ratio between the molar flux of gas product in bubbles and the theoretical gas production rate. A step-by-step derivation of η_{bub} is provided in Supplementary note 2. Fig. 2f shows that η_{bub} for O_2 decreases by 50 %, i.e., from ~ 0.7 at 1 bar to ~ 0.35 at 2 bar. For the case of H_2, $\eta_{bub} \approx 0.5$ at 1 bar, and it is reduced by ~ 20 % to ~ 0.4 at 2 bar. This η_{bub} trend aligns very well with the observed reduction in bubble-induced optical loss at higher pressures. Therefore, the reduction in optical losses at elevated pressure is due not only to the smaller bubble size resulting from pressurization, but more importantly, to the reduced fraction of gas that evolves into bubbles (as indicated by η_{bub}).

To assess the applicability of our findings to practical PEC water splitting cells, we performed additional experiments using a $BiVO_4$ photoanode as the working electrode. The rest of the experimental setup was kept identical to that shown in Fig. 1 and Fig. S1. The $BiVO_4$ photoanode was prepared using a previously reported electrodeposition method [43,44]. Oxygen bubble evolution was controlled by galvanostatic operation at 2.0 mA cm^{-2} in a 0.1 M KB_i (pH 9) buffer solution, while the operating pressure of the cell was varied from 1 bar to 4 bar by supplying high-pressure N_2 gas. The oxygen bubbles were monitored using the shadowgraphy method. Optical transmission measurement is unfortunately not feasible due to the near opacity of the $BiVO_4$ samples (see the digital photograph in Fig. S4c). Representative images from bubble shadowgraphy are shown in Fig. S4a, with the corresponding histograms of gas bubble size (D_{bub}) presented in Fig. S4b. The results indicate that the oxygen gas bubbles evolved from the $BiVO_4$

photoanode exhibit similar response to pressurization as those observed with the Pt mesh electrode, as shown by the reduced D_{bub} as pressure increases in Fig. S4b. This confirms that the pressure-dependent bubble dynamics observed in our "dark" electrochemical water splitting cell (Fig. 1) are also applicable to practical PEC water splitting cells.

Our findings above suggest that an increase in operating pressure is highly beneficial since it reduces the optical losses and thereby improves the photoelectrode's performance. However, it must be realized that increasing the operating pressure will also increase the thermodynamic (Nernstian) cell voltage. We therefore evaluated the effect of pressure on the cell potential at a current density of 2.5 mA cm^{-2} in 2 M KP$_i$ (pH = 7) electrolyte. Prior to the measurement, the electrolyte was purged and pressurized with N_2 gas. The cell potential increase (compared to that at 1 bar) with pressure is plotted in Fig. 3. For reference, we also plot the theoretical Nernst potential increase with pressure based on the following equation: [45]

$$E^0_{cell}(p,T) = E^0(T) + \frac{R\ \ T}{z\ \ F}\ln\left(\frac{a(H_2)\ \ \sqrt{a(O_2)}}{a(H_2O)}\right) \tag{1}$$

where $E^0(T)$ is the temperature-dependent equilibrium potential, and z is the number of electrons involved in the electrochemical reaction (2 for hydrogen and 4 for oxygen). Since our measurement here focuses on the oxygen evolution reaction, the value of z that we used is 4. a is the activity of the redox species. For liquid water, $a(H_2O) = 1$, for H_2 and O_2 ideal gas behavior can be assumed [46,47], i.e., $a(H_2) = p_{H_2}$ and $a(O_2) = p_{O_2}$.

The observed increase in cell potential with increasing pressure (purple squares in Fig. 3) aligns well with the expected values based on thermodynamics (dashed line) up to 3 bar. The deviation at 4 bar is, however, unexpected. We suspect that this discrepancy is due to an overestimation of the partial pressure of gases in equation (1), as we assumed $p_{O_2} = p_{H_2} = p$, despite N_2 gas being used for purging and pressurizing. To verify this, we replaced the purging/pressurizing gas from N_2 to O_2. Indeed, the increase in cell potential (blue squares in Fig. 3) is higher than the value predicted by the Nernst equation. This can be attributed to supersaturated O_2 in the vicinity of the electrode, as the bulk electrolyte is saturated with O_2 at operating pressure. Nevertheless, it is important to note that the increase in cell potential is very small, ~10–15 mV at 4 bar, which is only ~ 1 % of the total cell voltage at 1 bar. Clearly, the benefits of the pressure-induced reduction of optical losses observed in our experiments (Fig. 2) significantly outweigh the slight increase in required cell voltage.

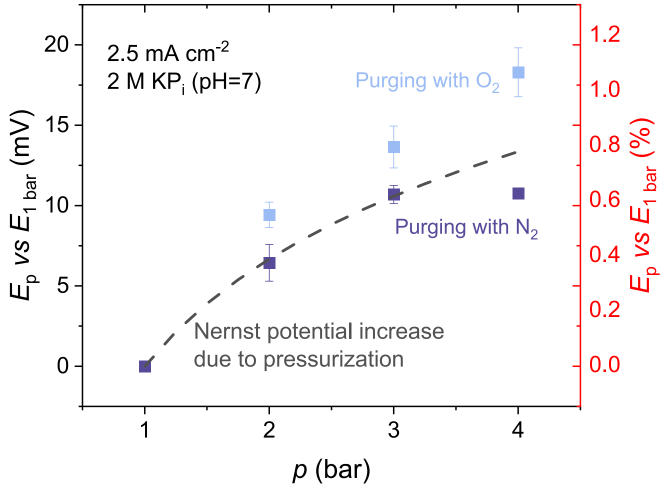

Fig. 3. Increase in cell potential (vs. potential at 1 bar) as a function of pressure. The pressure was increased by introducing N_2 or O_2 into the headspace of the cell (purple or blue squares, respectively), as illustrated in Fig. S1c. Introducing the gas via the headspace instead of bubbling it through the electrolyte greatly reduces fluctuations (noise) in the measured current. Error bars represent the standard deviation of at least three tests. The dashed line represents the expected theoretical increase based on the Nernst equation (eqn (1)).

2.2. Effect of current density on the bubble-induced optical loss

We now discuss the influence of current density on the bubble-induced optical losses. The electrolyte was kept the same (2 M KP$_i$, pH = 7), while the current density was maintained at ± 1.2, ±1.9 and ± 2.5 mA cm^{-2}. The raw data of the optical power measurements are shown in Fig. S5, and the results are summarized in Fig. 4. Fig. 4a shows that the H_2 bubble-induced optical losses, as obtained from the optical power profile, increase with current density, irrespective of the operating pressure. This correlation can be attributed to the production of more bubbles with smaller sizes at higher current densities (see Fig. 4b), despite having the same total volume of H_2 gas evolving as bubbles (Fig. 4c). In other words, our results indicate that a larger number of small bubbles causes more severe optical loss than a smaller number of larger bubbles.

While our observation above seems intuitive, it contradicts previous studies that reported optical losses to increase with larger bubbles [32,33,48]. The discrepancy likely arises from the different types of bubbles investigated; our study focuses on the optical effects of mobile bubbles (i.e., a "bubble curtain") in the electrolyte, while the earlier studies investigated scattering from static bubbles adhering to the electrode surface. In real-world PEC systems, some bubbles will adhere at the (photo)electrode surface, whilst more bubbles will be mobile in the electrolyte due to gravity. Therefore, predictions based solely on the geometrical scattering from static bubbles may not be sufficient. More quantitative data on bubble populations and the associated optical losses are therefore required to further refine our understanding.

The correlation of O_2 bubble characteristics (D_{bub}, N_{bub}, and η_{bub}) and bubble-induced optical loss is shown in Fig. 4d-f. Interestingly, a different trend with respect to current density is observed compared to that of H_2 bubbles. Although the exact reason remains unclear, we propose two possible factors. First, at the same current density, the production rate of H_2 is twice of O_2 due to the number of electrons involved in the reaction. Second, H_2 bubbles are larger compared to O_2, as shown from the size difference in Fig. 4b and 4e. Since gas bubble detachment can influence local mass transport near the electrodes [27,35], the detachment of larger-sized H_2 bubbles will likely exhibit more pronounced effect on H_2 bubble evolution than O_2. As a result, the dependence between bubble characteristics (D_{bub} and N_{bub}) on the current density is more pronounced for H_2 than O_2.

2.3. Effect of electrolyte concentration on bubble-induced optical loss

As bubble dynamics can be greatly influenced by electrolyte concentration [49], the effect of electrolyte concentration on bubble-induced optical loss has to be discussed. Three different concentrations of KP$_i$ buffer (pH 7) were used as the electrolyte (0.5 M, 1 M and 2 M), and the current density was fixed at ± 2.5 mA cm^{-2}. The H_2 and O_2 bubble-induced optical losses in these electrolytes are shown in Fig. 5a and 5b, respectively (see Figs. S6 and S7 for the optical power profiles). As shown, the electrolyte concentration significantly affects the bubble-induced optical losses. For example, under H_2 evolution at 1 bar, the losses were reduced from ~ 20 % to ~ 5 % and then to ~ 3 % as the KP$_i$ concentration decreased from 2 M to 1 M and then to 0.5 M KP$_i$ (see Fig. 5a). The same trend, although a little less pronounced, is also seen for O_2 evolution. This reduction in bubble-induced optical scattering can be attributed to the generation of fewer but larger bubbles with decreasing KP$_i$ buffer concentration (see Fig. 5c and 5d for H_2 and O_2 bubbles, respectively). For example, at 1 bar, the average H_2 bubble diameter increases more than 3-fold (from 55 μm to 180 μm) and N_{bub} decreases more than 50-fold (from ~ 1400 to ~ 25) when the concentration of KP$_i$ decreases from 2 M to 0.5 M. These findings suggest that

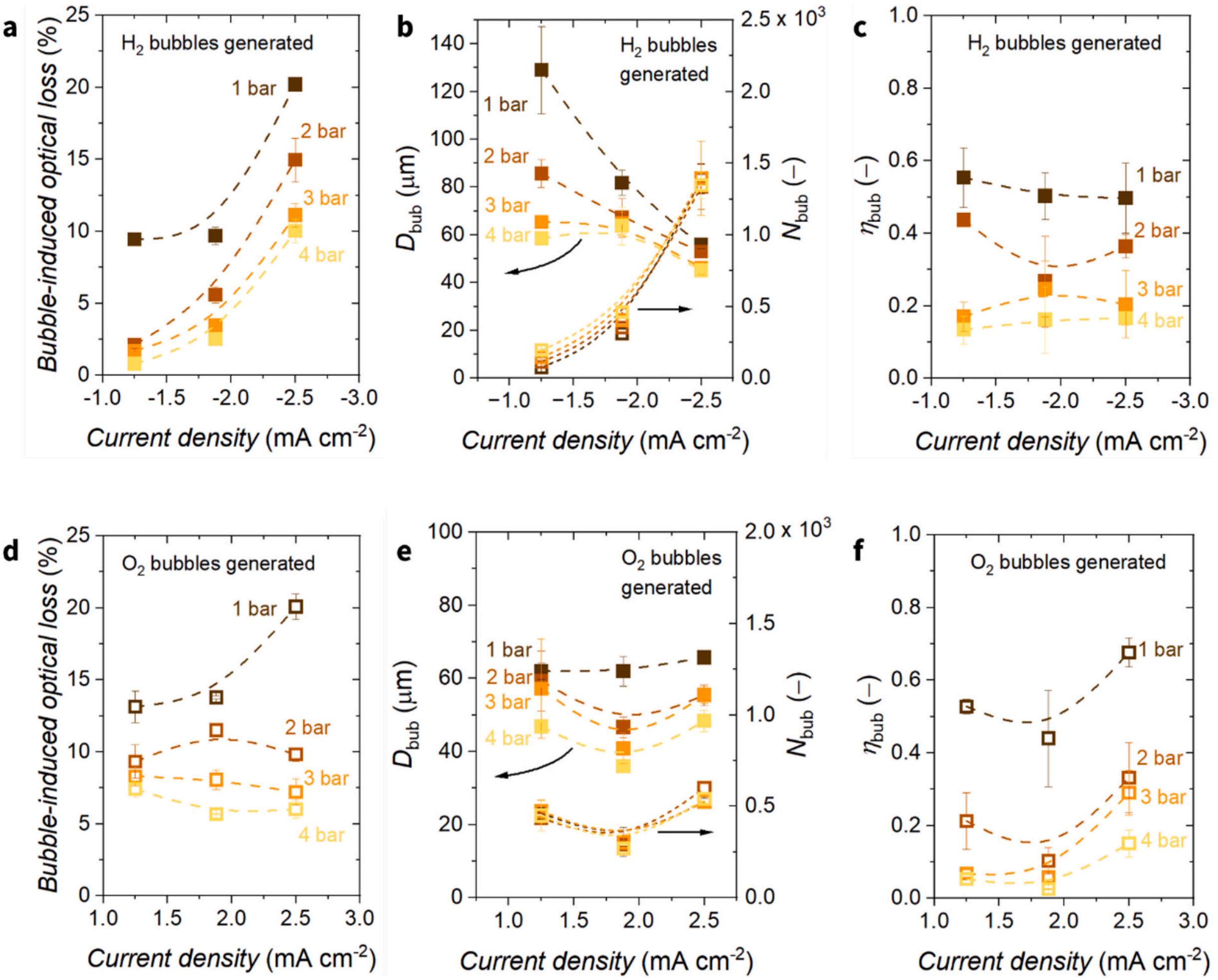

Fig. 4. Effect of current density on the bubble induced optical loss and the bubble properties. (a) H_2 bubble-induced optical loss, (b) shows the average H_2 bubble diameter and number of H_2 bubbles, (c) H_2 bubble formation efficiency. (d)-(f) show the same as (a)-(c) but for O_2. The electrolyte was 2.0 M KP_i (pH = 7), Pt mesh was the working electrode, Ag/AgCl was the reference electrode, and Pt wire was the counter electrode. The current densities tested were ± 1.2, ±1.9, and ± 2.5 mA cm^{-2}. Error bars represent the standard deviation of at least three tests.

optical losses from scattering at bubbles can be greatly reduced by decreasing the KP_i buffer concentration. However, it should be noted that this strategy comes at the expense of higher ohmic losses, as more diluted electrolytes has lower ionic conductivity [14,50]. Moreover, pH gradient-induced overpotentials are expected to be higher at lower buffer concentrations [51]. An optimum concentration likely exists, and the role of electrolyte engineering is, therefore, crucial in minimizing the total losses. Determining the optimal electrolyte concentration for PEC water splitting may require statistical methods, such as machine learning (ML)-based algorithms. More reliable experimental and simulation data are also needed to ensure that these ML models would be accurate.

The decrease of average bubble diameter (Fig. 5c and d) with increasing KP_i buffer concentration is consistent with another study by Qiu et al. that reported oxygen bubble evolution from nickel foil electrodes [49]. The authors used existing model to elucidate the underlying factors [52], and they concluded that the increase in surface tension coefficient, electrolyte density, and hydrophilicity of the Ni electrode during water electrolysis are responsible for the reduced bubble diameter at higher electrolyte concentration. To check whether the same explanation can also be used for our observation, we measured the physical properties of our KP_i buffer solutions. The results are shown in Fig. S8a-c, and the reported physical properties for electrolytes used in the study of Qiu et al. are added for comparison [49]. Indeed, the trends of electrolyte density, surface tension coefficient, and dynamic viscosity for our KP_i buffer solution are similar to those reported by Qiu and coauthors [49]. Furthermore, their measurements revealed that the bubble diameter exhibit similar dependence on the electrolyte concentration across different electrolytes, including K-borate, K-carbonate, KOH, and K-phosphate (see Fig. 1e in Ref. [49]). This also suggests that although our study focuses on the use of KP_i buffer, the findings are likely applicable to different types of near-neutral pH electrolytes, e.g., potassium borate (KB_i) and potassium carbonate (KC_i), and alkaline electrolytes like KOH.

We summarize our findings in Fig. 6. The D_{bub} measured from various experiments are plotted against the respective N_{bub}, and the color of each datapoint corresponds to the bubble-induced optical losses. The data are categorized based on the type of gas bubbles (H_2 or O_2) and the electrolyte concentration used in the experiment. Several general observations can be highlighted here. First, no apparent difference can be seen for H_2 vs. O_2, which signifies the generality of the observed trend. Second, the plot shows that having many small bubbles (bottom right region) is more detrimental to the performance in terms of optical losses than having fewer large bubbles (top left region). Third, modifying the electrolyte concentration is an effective strategy for altering the bubble characteristics; higher KP_i concentrations tend to generate a lot of small bubbles, while lower KP_i concentrations generate bigger but fewer bubbles. Other parameters that we investigated here (i.e., pressure, current density) also affect the bubble-induced optical losses, although their impact appears to be less universal than that of

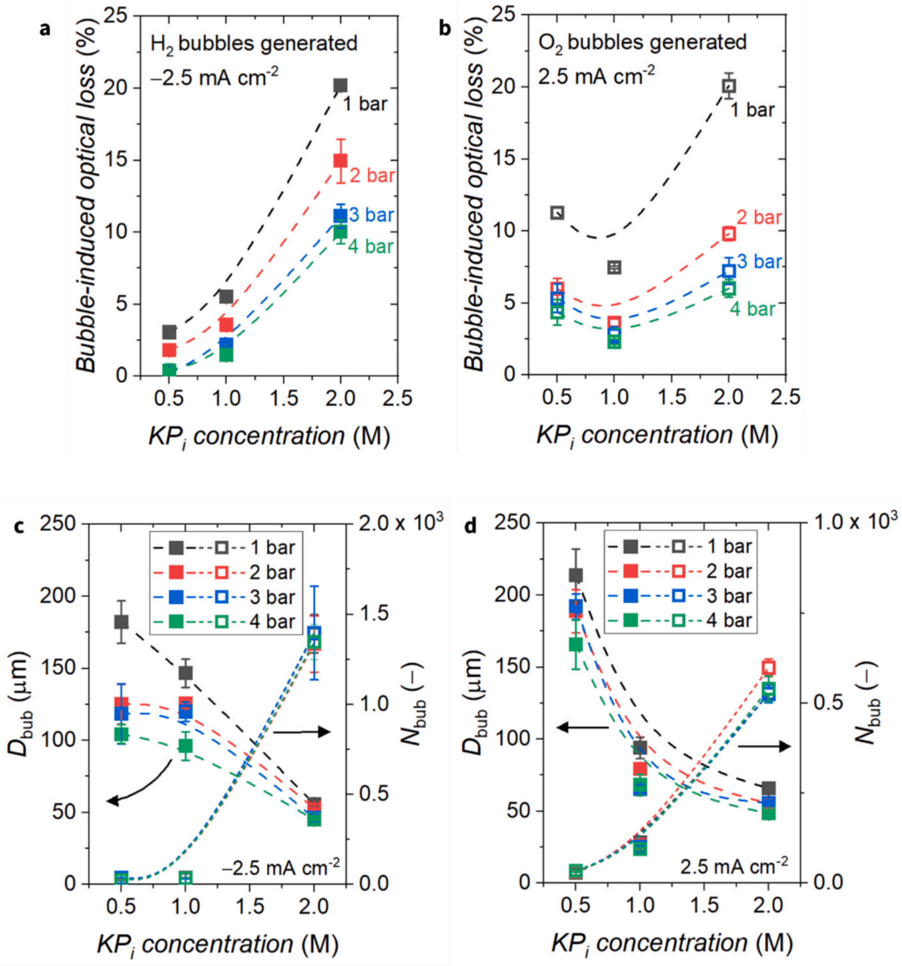

Fig. 5. (a) H_2 and (b) O_2 bubble-induced optical losses in potassium phosphate (KP_i) buffered electrolytes of varying concentrations. (c) The average H_2 bubble diameter (D_{bub}) and the number of H_2 bubbles per frame (N_{bub}) as a function of KP_i buffer concentration. (d) D_{bub} and N_{bub} for O_2 as a function of KP_i buffer concentration. The pH of all the electrolytes used was kept at 7. Bubble evolution was controlled by galvanostatic operation at current density of ± 2.5 mA cm^{-2}. Ag/AgCl was used as the reference electrode, Pt mesh was the working electrode, and Pt wire was used as the counter electrode. Error bars represent the standard deviation of at least three tests.

electrolyte concentration (see Fig. S9).

We acknowledge that several factors that may also be of importance are not discussed in this study. For example, the wettability (or hydrophobicity) of the (photo)electrode significantly affects bubble evolution. In (dark) electrolysis, it is well-established that large bubbles adhering on electrodes lead to higher kinetic overpotentials, thus lowering the electrochemical cell efficiency [24,25,53]. However, in photoelectrochemical water splitting, as suggested from Fig. 6, fewer large bubbles result in lower optical scattering losses. Therefore, the wettability of the photoelectrode should be carefully engineered to compromise between these different aspects and minimize the bubble-induced losses in PEC water splitting. Surface engineering approaches may be required to tailor the local wettability of the photoelectrode, which would allow decoupling of the gas evolution sites (oxygen or hydrogen evolution) from the bubble growth sites. Strategies to achieve this includes, but are not limited to, laser structuring of the top surface [54], the application of an organic protection layer with tunable wettability [55], or the use of selective masking during the deposition of electrochemical catalyst [56]. Such special-engineered photoelectrodes, although not trivial to obtain, can serve as a model system to study bubble dynamics in PEC water splitting, including nucleation, growth, coalescence, detachment, and mass transfer between the supersaturated dissolved gas boundary layer and the gas bubbles [40–42]. These insights will contribute to a deeper understanding of the relationship between bubble behavior and its impact on photoelectrochemical performance.

Furthermore, the effect of multiple gas bubbles adhering on photoelectrodes has not been considered in the present work; it has been suggested that they might act as light concentrator and lead to enhanced photo corrosion at particular locations [35]. Investigating this effect with our experimental setup is not possible, and the use of more advanced methods, e.g., scanning photocurrent microscopy (SPCM) [33], are required, which is beyond the scope of our study. Other factors not yet considered here are the orientation of the electrode and electrolyte flow. Our experiments were carried out in a batch cell, with the working electrode placed vertically. The inclusion of forced convection of the electrolyte, and/or the different inclination angle of the electrode could also play a critical role in affecting the bubble size distribution [38], the thickness of the bubble plume [26], and ultimately also the bubble-induced losses.

Finally, it is worth noting that pressurization in our cell was done by supplying high-pressure gas (N_2 or O_2) for practical reason, i.e., in order to shorten the experimental time. Future PEC water splitting cells should be designed to be “self-pressurizing” through the build-up of evolved gases (H_2 and O_2). In such systems, potential challenges such as oxygen crossover and high water vapor content may contaminate the produced high-pressure hydrogen. Solutions for gas purification can be adapted from existing technologies used in commercial water electrolyzers.

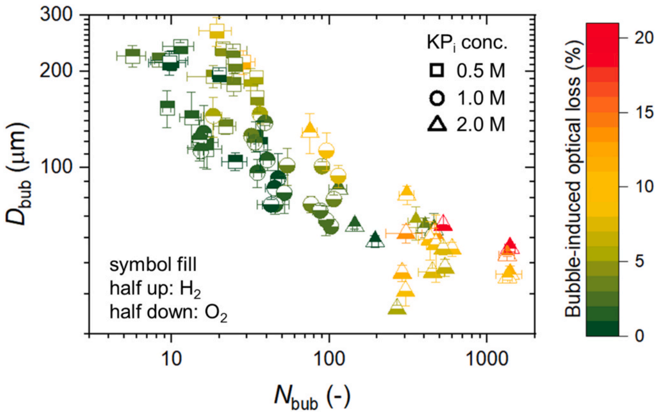

Fig. 6. The average bubble diameter (D_{bub}) vs. the number of bubbles per frame (N_{bub}) measured under various conditions, with the color scale representing the bubble-induced optical losses. Bubble evolution was controlled by galvanostatic operation at current densities of ± 1.2, ±1.9 and ± 2.5 mA cm^{-2}. Ag/AgCl was used as the reference electrode, Pt mesh was the working electrode, and Pt wire was used as the counter electrode. Electrolyte buffer concentrations of 0.5 M, 1 M and 2 M KP_i were used. Results for H_2 bubbles are shown as symbols with the upper half filled, while the O_2 bubble results are shown as symbols with the bottom half filled. Error bars represent the standard deviation of at least three tests.

Additionally, while operating PEC water splitting cells at elevated pressure indeed offers several benefits such as the minimized bubble-induced optical loss, additional challenges and costs related to cell design and maintenance may be introduced. These include the need for thicker glass compartment and more advanced sealing techniques to prevent electrolyte and gas leakage. A thorough techno-economic assessment is necessary to evaluate the feasibility of operating PEC water splitting systems at higher pressures.

3. Conclusion

In summary, direct optical power measurements and bubble shadowgraphy allow us to quantitatively correlate bubble-induced optical losses with key bubble characteristics, including average bubble diameter (D_{bub}), number of bubbles (N_{bub}), and bubble formation efficiency (η_{bub}). The evolution of O_2 and H_2 bubbles was studied under galvanostatic operation of a (photo)electrochemical water splitting cell at current densities of ± 1.2, ±1.9, and ± 2.5 mA cm^{-2}, using an aqueous electrolyte with various concentrations of potassium phosphate buffer (KP_i, pH = 7). Operating the cell at elevated pressure, up to 4 bar, resulted in a significant reduction of the bubble-induced optical losses: from 20 % at 1 bar to 10 % for H_2 bubbles and 6 % for O_2 bubbles at 4 bar. Notably, the increase in pressure only incurred a small thermodynamic penalty of ∼ 10–15 mV. Moreover, our study also showed that decreasing the KP_i buffer concentration strongly reduces the number of bubbles and increases the average bubble diameter, leading to a significant reduction of bubble-induced optical losses. Overall, our findings provide strategies for optimizing (photo)electrochemical water splitting cell designs and advance the development of highly efficient PEC systems.

4. Methods

4.1. (Photo)electrochemical water splitting cell at elevated pressure

A customized (photo)electrochemical cell was 3D-printed using semi-transparent heat-resistant plastic (VisiJet M2S-HT90). The cell has an internal volume of ∼ 120 ml, with an active electrode area of 2 cm × 2 cm. This cell was operated safely up to a pressure of 4 bar(a). The entire pressurized setup was placed under a protective shield for added safety, while the shield also serves to minimize stray light (see the black background in Fig. S1). The technical drawing of this cell is available from the corresponding author upon reasonable request. A platinum gauze (45 mesh woven from 0.198 mm dia. wire, 99.9 %, Thermo Fisher Scientific) was used as the working electrode in our experiments, and a platinum wire (0.1 mm dia. wire, 99.99 %, Thermo Fisher Scientific) was used as the counter electrode. The platinum mesh was electrochemically conditioned before every measurement by applying 30 cycles of cyclic voltammetry in potassium phosphate buffer (KPi, pH = 7) at various concentrations. The scanning range was from −0.65 V to 1.1 V vs. Ag/AgCl, with a scan rate of 0.1 V s^{-1}. The counter electrode (Pt wire) was bent into a special shape to avoid the bubble that evolve from it to obstruct the observation. Details are shown in the schematic illustrations in Fig. 2b and c, and digital photographs of the setup in Fig. S1b. A miniature Ag/AgCl electrode was purchased from Palmsens and used as the reference electrode. Electrical connections were made using copper wires, and the contacts were sealed with epoxy (101RF, purchased from Microset) to prevent any contact with the electrolyte. After the electrical connection was made, the glass windows (front and back, see Fig. 2a) were installed. A rubber O-ring, silicon glue (CHT SILCOSET 153, purchased from Farnell GmbH) and a pair of 3D-printed clamps were used to seal the device, as shown in the photographs in Fig. S1. No leakage occurred when the cell was operated at elevated pressure up to 4 bar. Potassium phosphate (KP_i) buffer solutions were prepared from KH_2PO_4 (Sigma-Aldrich, ≥99.0 %) and $K_2HPO_4·3H_2O$ (Sigma Aldrich, ≥99.0 %) to obtain the desired pH (7) and electrolyte concentrations. The water used in all experiments was obtained from a Milli-Q Integral system with a resistivity of 18.2 MΩ cm. The water splitting cell was pressurized by feeding N_2 or O_2 into the cell while controlling the mass flow rate at the cell outlet using a pressure controller (Bronkhorst High-Tech, uncertainty: 0.2 %). Electrochemical measurements were performed in the three-electrode configuration using a VersaSTAT 3 potentiostat/galvanostat (AMETEK).

4.2. Optical power measurement

The schematic illustration of our optical power measurement setup is shown in Fig. 2a, and a digital photograph of the setup is shown in Fig. S1. A solar simulator (Wacom-WXS-100S-L2H AM 1.5GMM) was used to as the light source. A thermopile sensor and controller (S401C and PM100D, Thorlabs) was used to measure the power of light transmitted through the electrochemical water splitting cell. The wavelength and power range of the thermopile sensor are 190 nm – 20 µm and 10 µW – 1 W (resolution = 1 µW), respectively. In order to avoid edge effects, an iris diaphragm (ID12/M, Thorlabs) was placed in front of the Pt mesh and kept with an opening diameter of 5 mm. This opening size was chosen so that averaged scattering measurements could be done over maximum illuminated area (instead of only localized scattering) while avoiding accumulated bubbles at the edge of the electrodes. Each optical power measurement was only recorded after the reading from the power meter reaches the equilibrium value, see Fig. S10. The optical power at this equilibrium is defined as the *background optical power*.

4.3. Bubble observation in a pressurized water-splitting cell

O_2 and H_2 bubbles were recorded using a shadowgraphy setup from LaVision. A solar simulator (Wacom-WXS-100S-L2H AM 1.5GMM) was used to illuminate the electrodes, while a neutral density (ND) filter (CFS1 filter mount with two CFS1-F1 modular inserts, Thorlabs) was placed in front of the camera (2752 × 2200 pixels) to prevent over-saturation (see the schematic shown in Fig. 2b). The three-electrode setup is configured the same as for the electrochemical measurements. Shadowgraphs of O_2 or H_2 bubbles were recorded chronologically (1 frame per second, fps) during the (constant current) electrochemical measurements. The cell pressure was increased stepwise, and sufficient time was given for the system to stabilize before the next pressure step.

An example of the chronopotentiometry plot is shown in Fig. S3a. The images were processed and analysed using ImageJ. A set of example images of the captured O_2 bubbles is shown in Fig. S3c. The bubble diameter (D_{bub}) and the number of bubbles (N_{bub}) were measured by averaging data from various bubble shadowgraphs (at least 5 frames) at the equilibrated stages of the chronopotentiometry. DaVis 10 software (LaVision) was used for bubble identification, but we always manually verify the assignments to check for errors and ensure accuracy. These parameters were then used to calculate the bubble formation efficiency, η_{bub}, following the method described in Supplementary Note 2. Other important bubble parameters, such as the rising velocity of gas bubbles (V_{bub}), can also influence the light transmittance. Larger bubbles turn to rise faster, thereby blocking light for a shorter duration. Quantifying V_{bub} from our experimental setup is challenging for two main reasons. First, the relatively low frame rate (1 fps) used in our measurements makes it difficult to track the same bubble across consecutive frames. Second, the shadowing effect from the Pt woven electrode further complicates bubble tracking. Nonetheless, we identified two representative gas bubbles of different sizes and observed that, as expected, the larger bubble rises faster than the smaller one in the electrolyte, as shown in Fig. S11. Future experiments should be conducted to investigate the effect of bubble residence time on optical transmittance.

CRediT authorship contribution statement

Feng Liang: Writing – review & editing, Writing – original draft, Visualization, Methodology, Investigation, Conceptualization. **Roel van de Krol:** Writing – review & editing, Supervision, Funding acquisition. **Fatwa F. Abdi:** Writing – review & editing, Supervision, Methodology, Funding acquisition, Conceptualization.

Declaration of competing interest

The authors declare that they have no known competing financial interests or personal relationships that could have appeared to influence the work reported in this paper.

Acknowledgements

We gratefully acknowledge the Helmholtz Association of German Research Centers (HGF) and the Federal Ministry of Education and Research (BMBF), Germany for supporting the development of solar powered technologies for H_2 generation within the framework of the Innovation Pool project “Solar H_2: Highly Pure and Compressed” and the Helmholtz Research Program “Materials and Technologies for the Energy Transition” (MTET). Part of the work was also carried out with the support of the Helmholtz Energy Materials Foundry (HEMF), a large-scale distributed research infrastructure founded by the German Helmholtz Association (GZ 714-48172-21/1). We also acknowledge Karsten Harbauer for his assistance in the preparation of Pt/FTO electrodes, Christian Höhn and Markus Bürger for the construction of the pressurized water splitting cell, Dr. Matias Berasategui, Heejung Kong, and Diwakar Suresh Babu for their assistance during the preparation of setup and the fruitful discussions. We acknowledge Dr. Babu Radhakrishnan for measuring the physical properties of the KP_i buffer solutions. F.F.A. also acknowledges support from CityUHK (project 9610621) and the Hong Kong Research Grant Council (RGC) under the ANR/RGC Joint Research Scheme (project A-CityU102/24).

Appendix A. Supplementary data

Supplementary data to this article can be found online at https://doi.org/10.1016/j.cej.2025.162513.

Data availability

Data will be made available on request.

References

[1] N.S. Lewis, Research opportunities to advance solar energy utilization, *Science* 351 (2016) aad1920.

[2] F.F. Abdi, et al., Efficient solar water splitting by enhanced charge separation in a bismuth vanadate-silicon tandem photoelectrode, *Nat. Commun.* 4 (2013) 2195.

[3] R. Van de Krol, M. Grätzel, *Photoelectrochemical Hydrogen Production*, Vol. 90, Springer, 2012.

[4] W. Yang, R.R. Prabhakar, J. Tan, S.D. Tilley, J. Moon, Strategies for enhancing the photocurrent, photovoltage, and stability of photoelectrodes for photoelectrochemical water splitting, *Chem. Soc. Rev.* 48 (2019) 4979–5015.

[5] J. Wang, et al., Subsurface Engineering Induced Fermi Level De-pinning in Metal Oxide Semiconductors for Photoelectrochemical Water Splitting, *Angew. Chem. Int. Ed.* 62 (2023) e202217026.

[6] X. Wang, S. Ma, B. Liu, S. Wang, W. Huang, Imperfect makes perfect: defect engineering of photoelectrodes towards efficient photoelectrochemical water splitting, *Chem. Commun.* (2023).

[7] H. Choi, et al., Suppression of Undesired Losses in Organometal Halide Perovskite-Based Photoanodes for Efficient Photoelectrochemical Water Splitting, *Adv. Energy Mater.* 13 (2023) 2300951.

[8] K. Sun, et al., A stabilized, intrinsically safe, 10% efficient, solar-driven water-splitting cell incorporating earth-abundant electrocatalysts with steady-state pH gradients and product separation enabled by a bipolar membrane, *Adv. Energy Mater.* 6 (2016) 1600379.

[9] K.R. Tolod, S. Hernández, N. Russo, Recent advances in the BiVO4 photocatalyst for sun-driven water oxidation: top-performing photoanodes and scale-up challenges, *Catalysts* 7 (2017) 13.

[10] T. Liu, et al., Low catalyst loading enhances charge accumulation for photoelectrochemical water splitting, *Angew. Chem. Int. Ed.* 62 (2023) e202307909.

[11] S. Tembhurne, F. Nandjou, S. Haussener, A thermally synergistic photo-electrochemical hydrogen generator operating under concentrated solar irradiation, *Nat. Energy* 4 (2019) 399–407.

[12] C. Xiang, et al., Modeling, simulation, and implementation of solar-driven water-splitting devices, *Angew. Chem. Int. Ed.* 55 (2016) 12974–12988.

[13] S. Haussener, et al., Modeling, simulation, and design criteria for photoelectrochemical water-splitting systems, *Energ. Environ. Sci.* 5 (2012) 9922–9935.

[14] F.F. Abdi, R.R.G. Perez, S. Haussener, Mitigating voltage losses in photoelectrochemical cell scale-up, *Sustainable Energy Fuels* 4 (2020) 2734–2740.

[15] S.Y. Tembhurne, S. Haussener, Integrated Photo-Electrochemical Solar Fuel Generators under Concentrated Irradiation-Part I: 2-D Non-Isothermal Multiphysics Modelling, *J. Electrochem. Soc.* 163 (2016) H988.

[16] S. Tembhurne, S. Haussener, Integrated photo-electrochemical solar fuel generators under concentrated irradiation, *J. Electrochem. Soc.* 163 (2016) H988.

[17] A.M. Fehr, et al., Integrated halide perovskite photoelectrochemical cells with solar-driven water-splitting efficiency of 20.8%, *Nat. Commun.* 14 (2023) 3797.

[18] I. Holmes-Gentle, S. Tembhurne, C. Suter, S. Haussener, Kilowatt-scale solar hydrogen production system using a concentrated integrated photoelectrochemical device, *Nat. Energy* 1–11 (2023).

[19] V. Andrei, et al., Floating perovskite-BiVO4 devices for scalable solar fuel production, *Nature* 608 (2022) 518–522.

[20] H. Nishiyama, et al., Photocatalytic solar hydrogen production from water on a 100-m2 scale, *Nature* 598 (2021) 304–307.

[21] J. Jin, et al., An experimental and modeling/simulation-based evaluation of the efficiency and operational performance characteristics of an integrated, membrane-free, neutral pH solar-driven water-splitting system, *Energ. Environ. Sci.* 7 (2014) 3371–3380.

[22] J.A. Leistra, P.J. Sides, Voltage components at gas evolving electrodes, *J. Electrochem. Soc.* 134 (1987) 2442.

[23] R.H. Coridan, Z.G. Schichtl, T. Sun, K. Fezzaa, Inhibition of Tafel kinetics for electrolytic hydrogen evolution on isolated micron scale electrocatalysts on semiconductor interfaces, *ACS Appl. Mater. Interfaces* 8 (2016) 24612–24620.

[24] A.E. Angulo, D. Frey, M.A. Modestino, Understanding bubble-induced overpotential losses in multiphase flow electrochemical reactors, *Energy Fuel* 36 (2022) 7908–7914.

[25] A. Angulo, P. van der Linde, H. Gardeniers, M. Modestino, D.F. Rivas, Influence of bubbles on the energy conversion efficiency of electrochemical reactors, *Joule* 4 (2020) 555–579.

[26] K. Obata, A. Mokeddem, F.F. Abdi, Multiphase fluid dynamics simulations of product crossover in solar-driven, membrane-less water splitting, *Cell Rep. Phys. Sci.* 2 (2021) 100358.

[27] Y.B. Vogel, et al., The corona of a surface bubble promotes electrochemical reactions, *Nat. Commun.* 11 (2020) 6323.

[28] K. Obata, F.F. Abdi, Bubble-induced convection stabilizes the local pH during solar water splitting in neutral pH electrolytes, *Sustainable Energy Fuels* 5 (2021) 3791–3801.

[29] M.E. Ivanova, et al., Technological Pathways to Produce Compressed and Highly Pure Hydrogen from Solar Power, *Angew. Chem. Int. Ed.* (2023) e202218850.

[30] I. Holmes-Gentle, F. Bedoya-Lora, F. Alhersh, K. Hellgardt, Optical losses at gas evolving photoelectrodes: implications for photoelectrochemical water splitting, *J. Phys. Chem. C* 123 (2018) 17–28.

[31] I. Holmes-Gentle, F. Alhersh, F. Bedoya-Lora, K. Hellgardt, *Photoelectrochemical Solar Cells* (2018) 1–41.

[32] X. Hu, et al., Single photogenerated bubble at gas-evolving TiO2 nanorod-array electrode, *Electrochim. Acta* 202 (2016) 175–185.

[33] A.E. Dorfi, A.C. West, D.V. Esposito, Quantifying Losses in Photoelectrode Performance Due to Single Hydrogen Bubbles, *J. Phys. Chem. C* 121 (2017) 26587–26597.

[34] A. Bhanawat, K. Zhu, L. Pilon, How do bubbles affect light absorption in photoelectrodes for solar water splitting? *Sustainable Energy Fuels* 6 (2022) 910–924.

[35] P.A. Kempler, Z.P. Ifkovits, W. Yu, A.I. Carim, N.S. Lewis, Optical and electrochemical effects of H 2 and O 2 bubbles at upward-facing Si photoelectrodes, *Energ. Environ. Sci.* 14 (2021) 414–423.

[36] F. Liang, R. van de Krol, F.F. Abdi, Assessing elevated pressure impact on photoelectrochemical water splitting via multiphysics modeling, *Nat. Commun.* 15 (2024) 4944.

[37] S. Grigoriev, A. Kalinnikov, P. Millet, V. Porembsky, V. Fateev, Mathematical modeling of high-pressure PEM water electrolysis, *J. Appl. Electrochem.* 40 (2010) 921–932.

[38] C.W. Sillen, *The effect of gas bubble evolution on the energy efficiency in water electrolysis*, Eindhoven University of Technology, Netherlands, 1983.

[39] J. Haverkort, H. Rajaei, Voltage losses in zero-gap alkaline water electrolysis, *J. Power Sources* 497 (2021) 229864.

[40] F. Liang, R. van de Krol, F.F. Abdi, The influence of dissolved gas supersaturation on bubble detachment from planar (photo) electrodes, *Cell Rep. Phys. Sci.* 5 (2024).

[41] A. Raman, et al., Potential response of single successive constant-current-driven electrolytic hydrogen bubbles spatially separated from the electrode, *Electrochim. Acta* 425 (2022) 140691.

[42] A. Raman, et al., Investigating mass transfer around spatially-decoupled electrolytic bubbles, *Chem. Eng. J.* 477 (2023) 147012.

[43] T.W. Kim, K.-S. Choi, Nanoporous BiVO4 photoanodes with dual-layer oxygen evolution catalysts for solar water splitting, *Science* 343 (2014) 990–994.

[44] H. Kong, et al., Electrolyte selection toward efficient photoelectrochemical glycerol oxidation on BiVO 4, *Chem. Sci.* 15 (2024) 10425–10435.

[45] M. Suermann, T. Kiupel, T.J. Schmidt, F.N. Büchi, Electrochemical hydrogen compression: efficient pressurization concept derived from an energetic evaluation, *J. Electrochem. Soc.* 164 (2017) F1187.

[46] H. Ito, T. Maeda, A. Nakano, H. Takenaka, Properties of Nafion membranes under PEM water electrolysis conditions, *Int. J. Hydrogen Energy* 36 (2011) 10527–10540.

[47] R. Wiebe, V. Gaddy, The Solubility of Hydrogen in Water at 0, 50, 75 and 100 from 25 to 1000 Atmospheres, *J. Am. Chem. Soc.* 56 (1934) 76–79.

[48] F. Njoka, S. Mori, S. Ookawara, M. Ahmed, Effects of photo-generated gas bubbles on the performance of tandem photoelectrochemical reactors for hydrogen production, *Int. J. Hydrogen Energy* 44 (2019) 10286–10300.

[49] H. Qiu, et al., Quantitative Description of Bubble Formation in Response to Electrolyte Engineering, *Langmuir* 39 (2023) 4993–5001.

[50] I.Y. Ahmet, et al., Demonstration of a 50 cm 2 BiVO 4 tandem photoelectrochemical-photovoltaic water splitting device, *Sustainable Energy Fuels* 3 (2019) 2366–2379.

[51] K. Obata, R. Van De Krol, M. Schwarze, R. Schomäcker, F.F. Abdi, In situ observation of pH change during water splitting in neutral pH conditions: impact of natural convection driven by buoyancy effects, *Energ. Environ. Sci.* 13 (2020) 5104–5116.

[52] J. Li, et al., Wetting states and departure diameters of bubbles on micro-/nanostructured surfaces, *Langmuir* 38 (2022) 3180–3188.

[53] R. Iwata, et al., Bubble growth and departure modes on wettable/non-wettable porous foams in alkaline water splitting, *Joule* 5 (2021) 887–900.

[54] J. Heinrich, et al., Functionalization of Ti64 via Direct Laser Interference Patterning and Its Influence on Wettability and Oxygen Bubble Nucleation, *Langmuir* 40 (2024) 2918–2929.

[55] B. Wu, et al., Stable solar water splitting with wettable organic-layer-protected silicon photocathodes, *Nat. Commun.* 13 (2022) 4460.

[56] Y. Hu, et al., Material design and surface/interface engineering of photoelectrodes for solar water splitting, *Sol. RRL* 5 (2021) 2100100.